photonics

MDPI

Article

Optimization of Erbium-Doped Fiber to Improve Temperature Stability and Efficiency of ASE Sources

Jia Guo , Hao Zhang, Wenbin Lin and Wei Xu *

School of Mathematics and Physics, University of South China, Hengyang 421001, China; optics-guo@usc.edu.cn (J.G.); ddzhang95@163.com (H.Z.); lwb@usc.edu.cn (W.L.)
* Correspondence: weixu@usc.edu.cn

Abstract: The ASE (Amplified Spontaneous Emission) light source, based on erbium-doped fiber (EDF), is a broadband light source with advantages such as high power, excellent temperature stability, and low coherent light generation. It is widely used in the field of fiber optic sensing. However, traditional ASE sources suffer from temperature sensitivity and low efficiency, which can compromise the accuracy and stability of the output light's average wavelength. This study focuses on optimizing the erbium-doped fiber (EDF) to improve the temperature stability and efficiency of the ASE light source. Through simulations, we found that the appropriate doping concentration and length of the EDF are key factors in enhancing the stability and efficiency of the ASE source. Inorganic metal chloride vapor-phase doping combined with an improved chemical vapor deposition process was used to fabricate the erbium-doped fiber, ensuring low background loss, minimal OH^- absorption, and uniform distribution of the erbium ions in the core of the fiber. The optimized EDFs were integrated into the ASE source, achieving a power conversion efficiency of 53.6% and a temperature stability of 0.118 ppm/°C within the temperature range of −50 °C to 70 °C. This study offers a practical approach for improving the performance of ASE light sources and advancing the development of high-precision fiber optic sensing technologies.

Keywords: amplified spontaneous emission sources; erbium doped fiber; vapor phase doping; fiber optic gyroscopes

check for updates

Received: 27 December 2024
Revised: 22 January 2025
Accepted: 25 January 2025
Published: 27 January 2025

Citation: Guo, J.; Zhang, H.; Lin, W.; Xu, W. Optimization of Erbium-Doped Fiber to Improve Temperature Stability and Efficiency of ASE Sources. *Photonics* **2025**, *12*, 115. https://doi.org/10.3390/photonics12020115

1. Introduction

Amplified spontaneous emission (ASE) sources utilizing erbium-doped fiber (EDF) are extensively employed in fiber optic gyroscopes (FOGs) due to their high output power, broad spectral bandwidth, low coherence, and low shot noise limit [1–4]. Typical research related to ASE sources in the context of FOGs focuses on minimizing temperature sensitivity and maximizing power conversion efficiency [5–10]. Since the angular velocity measured by the FOG is proportional to the Sagnac phase shift, with a scale factor depending on the wavelength used, the stability of the ASE's mean wavelength emerges as the most critical variable [11]. For high-precision inertial navigation FOGs, the ASE source is usually required to have a temperature stability of a few parts per million per degree Celsius (ppm/°C) or better [1,12]. Power conversion efficiency is also an important parameter for ASE source. Enhancing power conversion efficiency can achieve higher output power with lower pump power, thereby optimizing the signal-to-noise ratio and detection accuracy of the FOG while maintaining low energy consumption [13]. Hence, improving the efficiency and stability of ASE sources has emerged as a pivotal concern in elevating FOG performance.

In most ASE sources, instability mainly arises from variations in pump diode properties (power, center wavelength, and polarization state), fiber components (the wavelength division multiplexer, bandpass filter, reflector and isolator), and the intrinsic thermal-dependent gain property of the EDF [14,15]. While the effects of the first two factors can be mitigated by optimizing pump parameters and employing high-performance fiber components, the instability of ASEs is primarily determined by the thermal properties of EDFs [15–17]. During EDF manufacturing, it is necessary to precisely control the concentration of doped ions and ensure their uniform distribution in the silica optical fiber, which helps reduce the stress mismatch between the fiber matrix and the doped ions caused by heat, thereby effectively improving the temperature stability of the EDF [17–20]. Extensive global research has focused on developing standardized, repeatable process technologies to improve the concentration accuracy and distribution homogeneity of rare-earth (RE) doped fibers. Several preform fabrication techniques, chiefly alterations of the modified chemical vapor deposition (MCVD) process, have been explored [21,22]. Among these, the solution doping (SD) and the metal chloride vapor phase doping (VPD) are the most prevalent techniques [21]. The SD method, favored for its easy ofimplementation and broad dopant selection, has been continuously optimized over many years [21]. However, fibers produced by this method often exhibit higher hydroxyl absorption and background loss [23]. In contrast, in the VPD process, REs and codopants are incorporated simultaneously with silica deposition, ensuring homogeneous dopant distribution [24]. The dopant concentration can also be precisely controlled by adjusting the carrier gas flow rate and the sublimator temperature [24,25]. Notably, the VPD process, conducted "in situ", avoids environmental contaminants such as dust and moisture typically introduced during the soaking and reinstallation phases of the SD method [21]. Hence, actively advancing VPD technology remains a potent approach for reducing background loss and OH^- absorption of EDF and holds promise in improving the mean wavelength stability and power conversion efficiency of ASE sources.

In this study, we developed an ASE model through simulations and determined that adjusting the Er^{3+} ion concentration and EDF length significantly improves ASE stability and efficiency. To validate the simulation results, an inorganic metal chloride VPD method combined with the MCVD process was employed to manufacture EDFs. After comparative experiments, demonstrated that this process yields EDFs with superior stability and higher efficiency compared to commercial EDFs fabricated by solution doping technique. By further fine-tuning the dopant concentration and the EDF length, we achieved temperature stability of 0.118 ppm/°C within the temperature range of −50 to 70 °C, and power conversion efficiency of 53.6% in the ASE source, meeting the requirements of high-precision FOGs. These results pave the way for developing high-quality EDF and high-performance ASE sources, potentially driving advancements in FOG technology.

2. Principles and Simulations

The Er^{3+} ions within the silica optical fiber can absorb and emit photons [20]. EDFs are typically described using a three-level energy diagram to describe possible transitions, consisting of the ground state, metastable state, and upper energy level [26]. The rate equations for ASE sources utilizing EDF pumped at 980 nm can be expressed as [27,28]:

$$\begin{aligned}\frac{dP^{\pm}_{ASE}(z,\lambda_k)}{dz} = &\pm P^{\pm}_{ASE}(z,\lambda_k)\Gamma_s(\lambda_k)\big[\sigma_s^e(\lambda_k)N_2 - \sigma_s^a(\lambda_k)N_1 \\ &-\alpha_s(\lambda_k)\big] \pm 2\Gamma_s(\lambda_k)\sigma_s^e(\lambda_k)N_2 h\nu_k\Delta\nu_k\end{aligned} \tag{1}$$

$$\frac{dP_p(z)}{dz} = P_p(z)\Gamma_p(\lambda_p)\left[\sigma_p^e(\lambda_p)N_2 - \sigma_p^a(\lambda_p)N_1 - \alpha_p(\lambda_p)\right] \tag{2}$$

where the $P_{ASE}^{\pm}(z,\lambda_k)$ represents the ASE power, and the $P_p(z)$ represents the pump power along the fiber length. $\alpha_p(\lambda_p)$ and $\alpha_s(\lambda_k)$ denote the fiber losses for the pump and signal, respectively. The overlap factors at the pump and signal wavelengths are denoted as $\Gamma_p(\lambda_p)$ and $\Gamma_s(\lambda_k)$, respectively. $\sigma_s^e(\lambda_k)$ and $\sigma_s^a(\lambda_k)$ represent the emission and absorption cross-sections at the signal wavelength λ_k. $\sigma_p^e(\lambda_p)$ and $\sigma_p^a(\lambda_p)$ represent the emission and absorption cross-sections at the pump wavelength λ_p. N_1 and N_2 are the Er ion numbers at the ground state and the metastable state respectively. $N = N_1 + N_2$ is the total number of Er ions. h represents the Planck constant. Because the forward and backward ASE noise spreads in a continuum wavelength range, the whole ASE spectrum has been divided in K slots having $\Delta\nu_k, k = 1,2,\ldots,K$, bandwidth and centered around ν_k of the signal λ_k. The emission cross-section and the absorption cross-section at signal and pump wavelengths are related with the McCumber equation expressed as:

$$\sigma^e(\lambda) = \sigma^a(\lambda)e^{\frac{hc}{kT}\left(\frac{1}{\lambda_0} - \frac{1}{\lambda}\right)} \tag{3}$$

where the λ_0 represents the wavelength at which the absorption cross-section equals the emission cross-section.

The dependence of the ASE spectrum on temperature is mainly due to the variation in the occupancy probability of Er^{3+} ions on the ground and metastable energy manifolds. The ground energy manifolds are composed of I broadened vibrating sub-levels having $i, i = 1,2,\ldots,I$. The metastable energy manifolds are composed of J sub-levels, having $j, j = 1,2,\ldots,J$. N_{1i} is the number of ions in the i^{th} ground state sublevel ($\sum_i N_{1i} = N_1$), and N_{2j} is the number of ions in the j^{th} excited state sublevel ($\sum_j N_{2j} = N_2$). The distribution of Er^{3+} follows the Boltzmann distribution [29]. The occupancy probability of the energy level with energy E is given by:

$$p(E) = e^{-\frac{E}{kT}} f(T) \tag{4}$$

where k is the Boltzmann constant and T is the temperature. $f(T)$ is the partition function dependent on temperature, which must satisfy the normalization condition:

$$\int_{E^L}^{E^H} \rho(E)p(E)dE = 1 \tag{5}$$

where $\rho(E)$ represents the energy density, which is the number of ions allowed at the energy level of E per unit volume. Considering the uniform energy density, in the case of $E^L = 0$, $E^H = \infty$, the partition function can be simplified as follows:

$$f(T) = \frac{C}{T} \tag{6}$$

where C is a constant. Therefore, the numbers of Er^{3+} ions in the i^{th} ground state sublevel and j^{th} excited state sublevel are:

$$N_{1i} = N_1\rho(E_{1i})p(E_{1i}) = N_1\rho(E_{1i})e^{-\frac{E_{1i}}{kT}}\frac{C}{T} \tag{7}$$

$$N_{2j} = N_2\rho(E_{2j})p(E_{2j}) = N_2\rho(E_{2j})e^{-\frac{E_{2j}}{kT}}\frac{C}{T} \tag{8}$$

The transitionof Er^{3+} ions at the excited state energy sublevel E_{2j} to the ground state energy sublevel E_{1i} produces signal wavelength λ_{ij}, satisfying:

$$E_{2j} - E_{1i} = \frac{hc}{\lambda_{ij}} \tag{9}$$

Commercial software OptiSystem designed by Optiwave Systems Inc. was employed to simulate the ASE spectra at different temperatures based on the Boltzmann distribution. From the spectrum data, the mean wavelength $\bar{\lambda}$ and spectral width $\Delta\lambda$ of the ASE spectrum is calculated as follows:

$$\bar{\lambda} = \frac{\sum P_{ASE}(\lambda_k) \cdot \lambda_k}{\sum P_{ASE}(\lambda_k)} \tag{10}$$

$$\Delta\lambda = \frac{\sum P_{ASE}(\lambda_k) \cdot \Delta\lambda_k}{\sum P_{ASE}(\lambda_k)^2 \cdot \Delta\lambda_k} \tag{11}$$

where $\Delta\lambda_k$ represents the wavelength interval of the signal λ_k. From the above derivation, it can be inferred that the mean wavelength of the ASE source is temperature-dependent, and does not change monotonically with temperature. In other words, an extremum exists in its variation with temperature, which may be crucial for improving the temperature stability of ASE sources. It is expected that this extreme value will appear within the operating temperature range of the FOG to obtain a stable ASE source, thereby realizing high-precision and high-stability operation of the FOG.

The optical path of the ASE source is shown in Figure 1. The 980 nm pump light emitted by the pump laser was launched into the EDF under test via one arm of the wavelength division multiplexer (WDM). An optical fiber isolator (ISO) was connected at the end of the EDF to prevent the reverse-transmitted light at the back-end optical path from being reflected back into the EDF to form lasing. The functions of the filter and reflector in the other arm of the WDM are respectively to obtain a symmetrical Gaussian spectral shape of the ASE source around 1530 nm and to reflect the signal light back to the EDF for re-amplification.

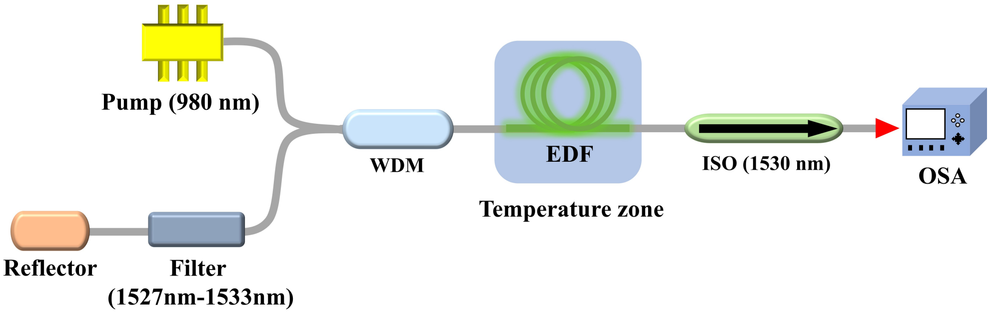

Figure 1. Schematic of the ASE sources.

EDF1, EDF2 and EDF3 were selected as candidates for this simulation. EDF1 was purchased from Fibercore (M-12 980/125). EDF2 and EDF3 were fabricated in-house by the inorganic metal chloride VPD technique with MCVD process. Among them, EDF2 has the same Er^{3+} ion concentration and density as EDF1. Table 1 details the specifications of all EDFs. Notably, the lengths of EDF1 and EDF2 are optimized to achieve the maximum output power of the ASE source under the same pump power. Through simulation, a peculiar phenomenon was discovered: the mean wavelength of the ASE source using EDF1 and EDF2 decreases initially, then increases with temperature within the range of −50 °C to 70 °C, reaching a minimum at about −18 °C, as shown in Figure 2. This phenomenon is consistent with our prior inference that the mean wavelength of the ASE source exhibits an extremum with temperature variation.

Table 1. Comparison of the three EDFS' parameters.

Parameters	EDF1	EDF2	EDF3
Numerical aperture (NA)	0.225	0.230	0.227
Peak Absorption at 1530 nm (dB/m)	18	23	9.8
Background Loss at 1200 nm (dB/km)	$\leq$10	5.05	5.54
Cutoff Wavelength (nm)	940	1220	970
Mode Field Diameter at 1550 nm (µm)	5.65	5.30	5.50
Erbium Ion Concentration (ppm)	2200	2200	1135
Erbium Ion Density ($1/m^3$)	1.74×10^{25}	1.74×10^{25}	0.9×10^{25}
Core Diameter (µm)	3.18	4.05	3.28
Cladding Diameter (µm)	125	125	125
Coating Diameter (µm)	245	245	245
Prooftest Level (kpsi)	200	200	200

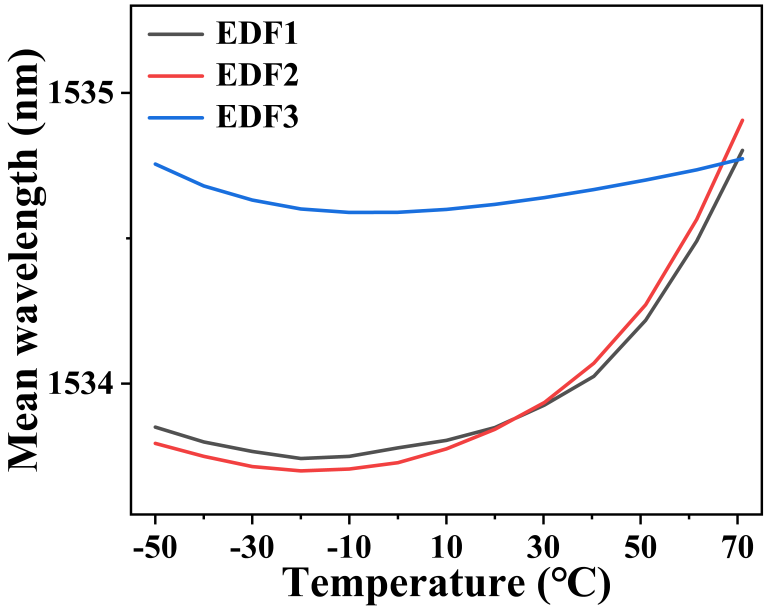

Figure 2. Simulation results for the mean wavelength variation with temperature for ASE sources utilizing EDF1, EDF2 and EDF3 of 6 m.

Additionally, through further altering the Er^{3+} ion concentration in the EDF, we found that when reducing the Er^{3+} ion concentration, although the mean wavelength exhibits a similar trend of first decreasing then increasing with temperature, the overall change is smoother. When the Er^{3+} ion concentration decreases to 0.9×10^{25} ($1/m^3$) and the EDF length is set to 6 m, the trend of mean wavelength variation with temperature is the gentlest (Figures 2 and 3), implying the best temperature stability. These simulation results suggest that the optimized EDF is anticipated to yield a temperature-stable ASE source. Subsequently, these results will be experimentally validated.

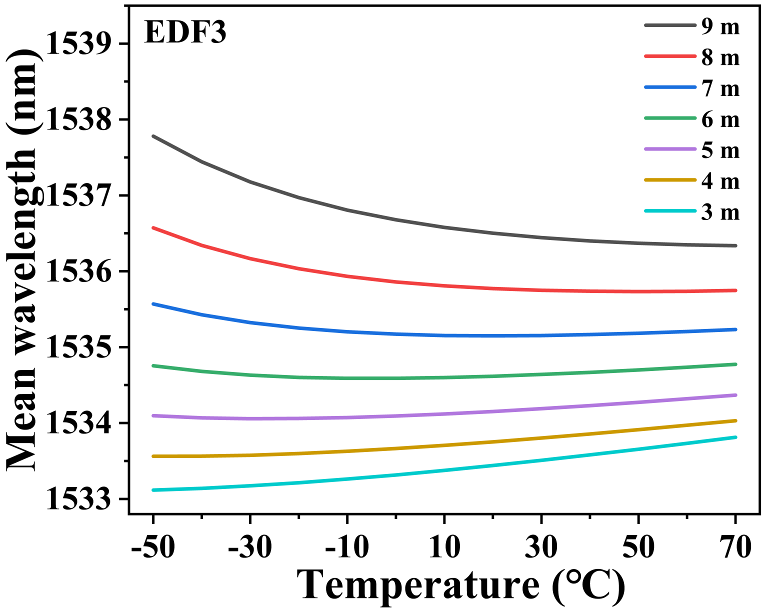

Figure 3. Simulation results of the mean wavelength variation with temperature for ASE sources utilizing EDF3 of different lengths.

3. Experimental Results and Discussion

It is important to note that only the EDF is placed in the temperature chamber (Manufacturer ATH-80L-6D), while the pump diode was kept at room temperature around 23.5 °C. The temperature change of all EDFs in this work is consistent, increasing from −50 to 70 °C with a fixed step change of 10 °C, maintain each temperature point for ten minutes to ensure stability, allowing a fair comparison of the ASE performance based on different EDFs. In order to increase the accuracy of the test, the spectral properties and output power of the ASE source were recorded after staying at each temperature for more than 10 min. The optical spectrum and output power of the ASE source were collected by an optical spectrum analyzer (OSA, Yokogawa AQ6370D) and a combination of power meter (HP 8153A) and detector (HP 81525A), respectively. An attenuator was employed before the output signal enters the OSA to prevent the power of the ASE source from exceeding the OSA power threshold.

The 2.13 m EDF1 and 2.5 m EDF2 were integrated into the optical path shown in Figure 1 for performance evaluation. As shown in Figure 4, the spectral characteristics of ASE sources utilizing EDF1 and EDF2 were obtained by sequentially splicing them into the optical path, with a pump power of 32 mW and within a temperature range of −50 to 70 °C. Figure 4a depicts the mean wavelength versus temperature across the entire temperature range. Notably, the mean wavelength of the ASE source utilizing EDF1 exhibits a continuous increment with rising temperature throughout the entire temperature span. However, for EDF2, the mean wavelength first decreases with temperature from −50 to −20 °C, and then increases with temperature from −20 to 70 °C. This phenomenon aligns with our prior derivations and simulation results.

Over the entire temperature range mentioned, the mean wavelength shift of the ASE source utilizing EDF1 is 31.5 ppm, whereas for EDF2 it is 20.35 ppm, as summarized in Table 2. The ASE source utilizing the VPD prepared EDF2 exhibits smaller mean wavelength shift, which may be due to the fact that the EDF manufacturing process proposed in this study can more effectively reduce the OH^- groups in the EDF compared with the traditional SD method, thereby enhancing the gain of the ASE [30]. Figure 4b illustrates the change of the spectral width of ASE sources utilizing EDF1 and EDF2 with temperature. It can be seen from the figure that the spectral width of the two ASE sources has the same trend with temperature, and the spectral width increases with temperature. By comparing the experimental results in Table 2, it is evident that, in comparison with EDF1, the VPD prepared EDF2 can better alleviate the spectral width variation of the ASE source.

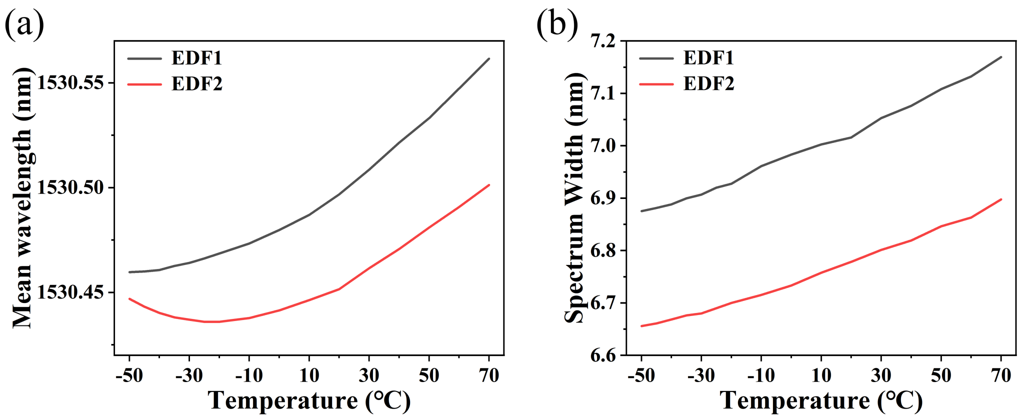

Figure 4. (**a**) Mean wavelength and (**b**) spectrum width as functions of temperature for ASE sources utilizing EDF1 and EDF2.

Table 2. Temperature stability and output characteristics of ASE sources utilizing EDF1 and EDF2.

	Mean Wavelength Shift (ppm)	Spectrum Width Change Rate (%)	Output Power Change Rate (%)	Power Conversion Efficiency (%)
EDF1	31.5	2.1	6	36.6
EDF2	20.35	1.8	5.8	40.03

Figure 5a depicts the output power versus pump power of the ASE sources utilizing EDF1 and EDF2 at room temperature. For the same pump power, the output power of the ASE source using EDF2 is approximately 20% greater than that of the ASE source using EDF1. For instance, at a pump power of 32 mW, the output power of the ASE source utilizing EDF2 is 10.16 mW, whereas that of the ASE source utilizing EDF1 is 8.33 mW. The power conversion efficiency of EDF2 is 40.03%, compared to only 36.6% for EDF1. These results indicate that the VPD fabrication process proposed herein enhances the power conversion efficiency of the ASE source. Figure 5b illustrates the output power variation of the two ASE sources with temperature at a constant pump power of 32 mW. Both curves exhibit a consistent trend, where the output power decreases with the increasing temperature. This could occur due to the elevated temperature intensifying thermal excitation, thermal quenching, and thermal broadening effects, leading to fewer Er^{3+} ions in the excited state, thus reducing the population inversion and weakening the output power of the ASE source [27,31]. The output power change rates of the ASE sources utilizing EDF1 and EDF2 across the entire temperature range were calculated to be 6% and 5.8%, respectively, which further proves that EDF2 has better temperature stability.

All the aforementioned experimental results confirm that the EDF manufacturing process developed in this study significantly improves the performance of the EDF, thereby optimizing the temperature stability and operational efficiency of the ASE source. Such optimization is essential for advancing high-precision FOG technology. Furthermore, the earlier simulation results suggest that further optimization of the ASE source is anticipated by adjusting the Er^{3+} ion concentration and the length of the EDF, which will be validated through subsequent experiments.

To validate the simulation results shown in Figure 3, the VPD method combined with the MCVD process was employed to fabricate EDF3. The mean wavelength variation of the

ASE source utilizing EDF3 with lengths from 3 to 9 m was measured across the temperature range of −50 to 70 °C at a pump power of 32 mW, as illustrated in Figure 6a. It becomes apparent that the experimental results closely resemble the simulated results, suggesting that the mean wavelength of the ASE source decreases as the length of EDF3 decreases. This occurs because shorter EDFs possess higher initial gains at shorter wavelengths, which quickly reach saturation, limiting the effective amplification of longer wavelengths [6,32]. Moreover, as temperature rises, ASE sources utilizing 3–5 m EDF3s typically exhibit an increase in mean wavelength, whereas those employing 7–9 m EDF3s tend to experience a decrease. Only ASE sources utilizing 6 m EDF3 demonstrate relative stability in mean wavelength, consistent with the previous simulation outcomes. Figure 6b depicts the correlation between the mean wavelength shift and EDF3 length, derived from Figure 6a data, providing additional confirmation for the simulations. Specifically, the ASE source employing 6 m EDF3 exhibits the lowest mean wavelength shift, approximately 14.2 ppm, as shown in Table 3. Consequently, the mean wavelength shift is notably reduced compared to ASE sources utilizing EDF1 and EDF2. This phenomenon is attributed to the disturbance caused by higher levels of doped ions within EDF1 and EDF2, leading to greater intrinsic instability, thereby complicating temperature control precision [12].

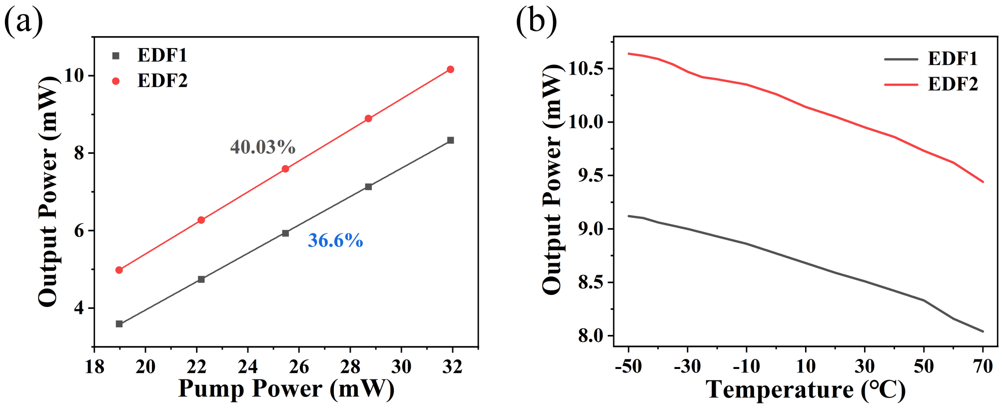

Figure 5. Comparison of output power between ASE sources utilizing EDF1 and EDF2. (**a**) Output power as a function of pump power; (**b**) Output power as a function of temperature.

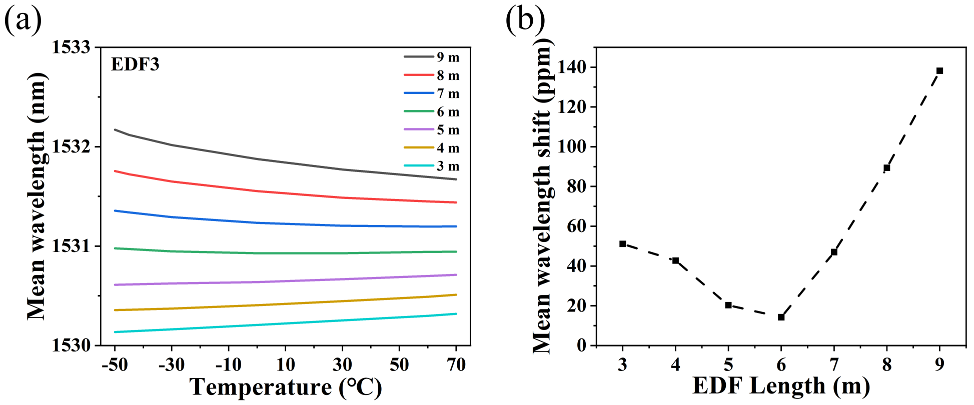

Figure 6. Mean wavelength temperature stability of ASE sources utilizing EDF3. (**a**) Variation of mean wavelength with temperature for ASE sources utilizing EDF3 of different lengths. (**b**) Dependency of the mean wavelength shift on the length of EDF3.

Figure 7 illustrates the variation of spectral width with temperature for ASE sources using different lengths of EDF3. While the spectral width of ASE sources utilizing all lengths of EDF3 increases with temperature, the specific trends vary. Calculations reveal the spectral width change rates of ASE sources for all lengths of EDF3, summarized in Table 3, with the lowest rate found for 6 m length of EDF3, approximately 1.3%.

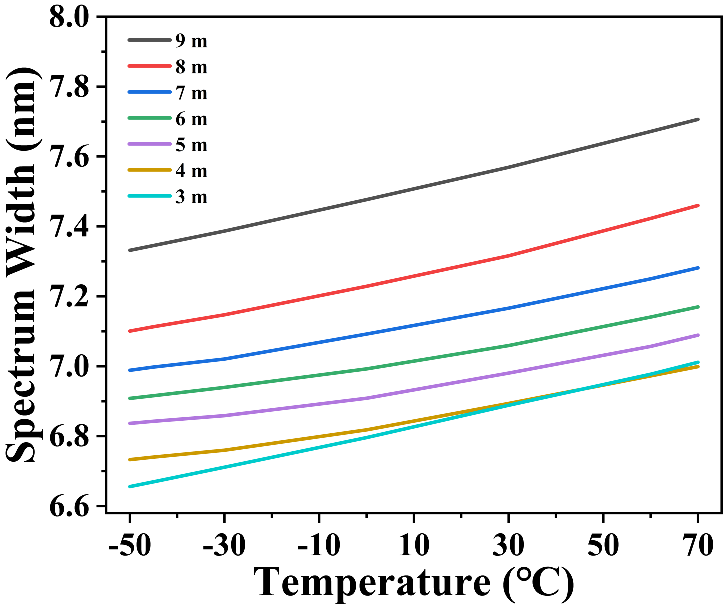

Figure 7. Variation of spectral width with temperature for ASE sources utilizing EDF3 of different lengths.

Table 3. Temperature stability and operational efficiency of ASE sources utilizing EDF3 with different lengths.

EDF3 Length (m)	Spectrum Width Change Rate (%)	Output Power Change Rate (%)	Power Conversion Efficiency (%)
3	51.1	2.3	23.05
4	42.7	1.7	40.73
5	20.3	1.5	50.84
6	14.2	1.3	53.6
7	47	1.8	53.31
8	89.4	2.1	52.67
9	138.2	2.2	51.53

Notably, the spectral profiles of ASE sources utilizing 2.13 m EDF1, 2.5 m EDF2, and 6 m EDF3 with respect to temperature are also recorded, as shown in Figure 8. The figure shows that the output spectra of the ASE source utilizing 6 m EDF3 varies minimally from −50 to 70 °C, further demonstrating that the temperature stability of the ASE source has been effectively improved.

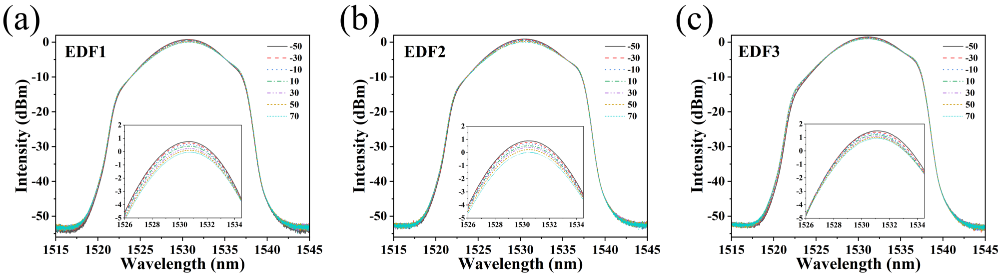

Figure 8. Variations in the output spectra of ASE sources utilizing (**a**) 2.13 m EDF1, (**b**) 2.5 m EDF2 and (**c**) 6 m EDF3 across the temperature range of −50 to 70 °C.

In addition to temperature stability, the power conversion efficiency of ASE sources is another crucial factor in assessing their suitability for high-precision FOGs. To further investigate the power conversion efficiency of ASE sources utilizing EDF3, the output power of ASE sources utilizing EDF3 with varying lengths was measured and recorded in Figure 9a. ASE sources using 6 m EDF3 were found to have a maximum output power of approximately 14.07 mW at a pump power of 32 mW. By performing linear fitting, the operational efficiency of ASE sources for various lengths of EDF3 was determined (Table 3), indicating that the 6 m EDF3 can achieve the highest efficiency of 53.6% for ASE sources. Finally, the impact of temperature variation on the output power of ASE sources was investigated at a pump power of 32 mW, with particular emphasis on EDF3 with a length of 6 m, as shown in Figure 9b. Similar to ASE sources utilizing EDF1 and EDF2, the output power decreases with rising temperature. However, ASE sources utilizing EDF3 exhibit the lowest output power change rate, at approximately 4.5%. These results suggest that selecting the appropriate length of the VPD fabricated EDF3 can significantly improve the maximum output power, operational efficiency, and power stability of ASE sources.

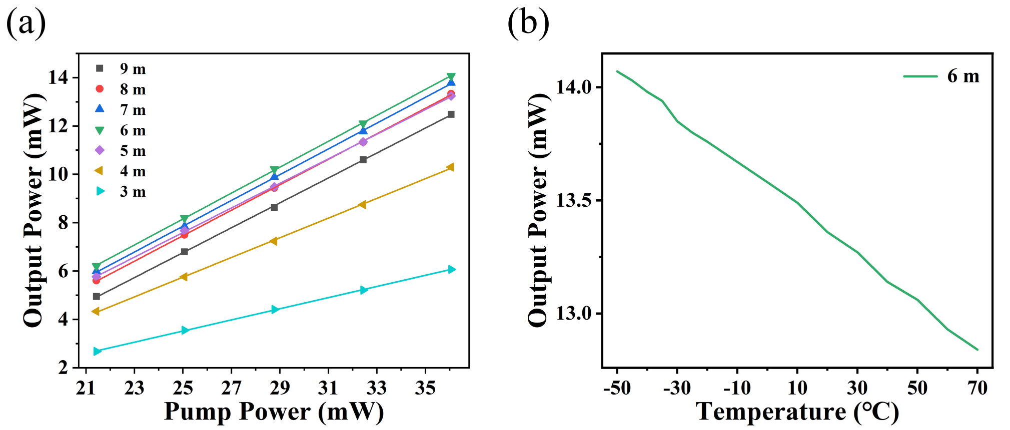

Figure 9. Output power of ASE sources utilizing EDF3 as a function of (**a**) pump power (3–9 m EDF3) and (**b**) temperature (6 m EDF3).

4. Conclusions

In summary, due to the low background loss, low OH^- absorption, and uniform distribution of Er dopants in EDFs produced by the VPD process, the temperature stability and operating efficiency of the ASE source have been significantly improved. Additionally, the performance of the ASE source was further optimized by adjusting the Er^{3+} ion concentration and the length of the EDF based on simulation results. When the Er^{3+} ion concentration was reduced to 0.9×10^{25} $(1/m^3)$ and the EDF length was set to 6 m, the conversion efficiency of the ASE source from pump light to output light reached 53.6 °C. The mean wavelength drift was only 14.2 ppm, i.e., 0.118 ppm/°C, within the temperature range of −50 to 70 °C. This research not only holds promise for addressing challenges in the current field of RE doped fibers but also serves as a key driver for advancing transformative progress in FOG technology.

Author Contributions: Conceptualization, W.X.; methodology, W.X.; formal analysis, W.X. and W.L.; investigation, J.G.; resources, W.X. and W.L.; data curation, H.Z. and J.G.; writing—original draft preparation, J.G.; writing—review and editing, W.X. and W.L.; visualization, J.G. and H.Z.; supervision, W.X.; project administration, W.X. All authors have read and agreed to the published version of the manuscript.

Funding: This work was partially funded by the National Natural Science Foundation of China under Grant 62205213, in part by the Fund of University of South China (Grant No. 231RGC011), and partially funded by the Fund of University of South China (Grant No. 231RGC010).

Institutional Review Board Statement: Not applicable.

Informed Consent Statement: Not applicable.

Data Availability Statement: Data is contained within the article.

Conflicts of Interest: The authors declare no conflicts of interest.

References

1. Song, N.; Xu, X.; Zhang, Z.; Gao, F.; Wang, X. Advanced interferometric fiber optic gyroscope for inertial sensing: A review. *J. Light. Technol.* **2023**, *41*, 4023–4034. [CrossRef]
2. Wang, Z.; Wang, G.; Kumar, S.; Marques, C.; Min, R.; Li, X. Recent advancements in resonant fiber optic gyro—A review. *IEEE Sens. J.* **2022**, *22*, 18240–18252. [CrossRef]
3. Lefèvre, H.C. The fiber-optic gyroscope: Challenges to become the ultimate rotation-sensing technology. *Opt. Fiber Technol.* **2013**, *19*, 828–832. [CrossRef]
4. Ciminelli, C.; Dell'Olio, F.; Campanella, C.E.; Armenise, M.N. Photonic technologies for angular velocity sensing. *Adv. Opt. Photonics* **2010**, *2*, 370–404. [CrossRef]
5. Petrov, A.B.; Gumenyuk, R.; Alimbekov, M.S.; Zhelezov, P.E.; Kikilich, N.E.; Aleynik, A.S.; Meshkovsky, I.K.; Golant, K.M.; Chamorovskii, Y.K.; Odnoblyudov, M.; et al. Broadband superluminescent erbium source with multiwave pumping. *Opt. Commun.* **2018**, *413*, 304–309. [CrossRef]
6. Zhu, L.; He, W.; Zhang, Y.; Luo, F.; Dong, M. A high flattening C+ L band broadband source based on single pump and the same erbium-doped fiber. *Optik* **2014**, *125*, 4659–4662. [CrossRef]
7. Liu, C.; Wu, X.; Zhu, J.; He, N.; Li, Z.; Zhang, G.; Zhang, L.; Ruan, S. Radiation-resistant Er3+-doped superfluorescent fiber sources. *Sensors* **2018**, *18*, 2236. [CrossRef]
8. Ponosova, A.A.; Azanova, I.; Mironov, N.K.; Yashkov, M.V.; Riumkin, K.E.E.; Sharonova, Y.O.; Melkumov, M. Erbium-doped optical fibre with enhanced radiation resistance for superluminescent fibre sources. *Quantum Electron.* **2019**, *49*, 693. [CrossRef]
9. Xie, L.; Gong, X.; Zhang, B.; Fan, X.; Zhang, C. Research on temperature dependent mean wavelength stability of Erbium-doped fiber super fluorescent source for fiber optic gyroscopes. In Proceedings of the AOPC 2017: Fiber Optic Sensing and Optical Communications, Beijing, China, 4–6 June 2017; pp. 388–393.
10. Wang, A.; Ou, P.; Feng, L.; Zhang, C.; Cui, X.; Liu, H.; Gan, Z. High-stability Er-doped superfluorescent fiber source incorporating photonic bandgap fiber. *IEEE Photonics Technol. Lett.* **2009**, *21*, 1843–1845. [CrossRef]
11. Skalský, M.; Hnidka, J.; Havránek, Z. Improvement of the Temperature Stability of the Erbium-Doped Superfluorescent Fiber Source by Tuning the Reflectivity of the Fiber End. *J. Light. Technol.* **2022**, *41*, 1843–1850. [CrossRef]
12. Wan, H.; Zhang, D.; Sun, X. Stabilization of a superfluorescent fiber source with high performance erbium doped fibers. *Opt. Fiber Technol.* **2013**, *19*, 264–268. [CrossRef]
13. Chen, X.; Ma, L.; Liu, B.-H.; Hao, Y. Design of ASE source for high precision FOG. In Proceedings of the AOPC 2019: Optical Fiber Sensors and Communication, Beijing, China, 5–8 August 2019; pp. 387–394.
14. Zhang, E.; Yang, L.; Xue, B.; Gao, Z.; Zhang, Y.; Yam, S.S.-H. High thermal-stability Er-doped superfluorescent fiber source with a vertical cleaved fiber tail. *Opt. Fiber Technol.* **2020**, *58*, 102262. [CrossRef]
15. Wysocki, P.F.; Digonnet, M.J.; Kim, B.Y.; Shaw, H.J. Characteristics of erbium-doped superfluorescent fiber sources for interferometric sensor applications. *J. Light. Technol.* **1994**, *12*, 550–567. [CrossRef]
16. Falquier, D.; Digonnet, M.; Shaw, H. A polarization-stable Er-doped superfluorescent fiber source including a Faraday rotator mirror. *IEEE Photonics Technol. Lett.* **2000**, *12*, 1465–1467. [CrossRef]
17. Wang, A. High stability Er-doped superfluorescent fiber source improved by incorporating bandpass filter. *IEEE Photonics Technol. Lett.* **2010**, *23*, 227–229. [CrossRef]
18. Wu, X.; Zhang, L.; Liu, C.-X.; Ruan, S.-C. High-stable, double-pass forward superfluorescent fiber source based on erbium-doped photonic crystal fiber. *Appl. Phys. B* **2014**, *114*, 433–438. [CrossRef]
19. Ou, P.; Cao, B.; Zhang, C.; Li, Y.; Yang, Y. Er-doped superfluorescent fibre source with enhanced mean-wavelength stability using chirped fibre grating. *Electron. Lett.* **2008**, *44*, 1. [CrossRef]
20. Giles, C.R.; Desurvire, E. Modeling erbium-doped fiber amplifiers. *J. Light. Technol.* **1991**, *9*, 271–283. [CrossRef]
21. Saha, M.; Sen, R. Vapor phase doping process for fabrication of rare earth doped optical fibers: Current status and future opportunities. *Phys. Status Solidi (a)* **2016**, *213*, 1377–1391. [CrossRef]

22. Sharif, K.M.; Omar, N.Y.; Zulkifli, M.; Yassin, S.M.; Abdul-Rashid, H. Fabrication of alumina-doped optical fiber preforms by an MCVD-metal chelate doping method. *Appl. Sci.* **2020**, *10*, 7231. [CrossRef]
23. Dhar, A.; Paul, M.C.; Pal, M.; Mondal, A.K.; Sen, S.; Maiti, H.S.; Sen, R. Characterization of porous core layer for controlling rare earth incorporation in optical fiber. *Opt. Express* **2006**, *14*, 9006–9015. [CrossRef] [PubMed]
24. Saha, M.; Pal, A.; Sen, R. Vapor phase doping of rare-earth in optical fibers for high power laser. *IEEE Photonics Technol. Lett.* **2013**, *26*, 58–61. [CrossRef]
25. Sekiya, E.; Barua, P.; Saito, K.; Ikushima, A. Fabrication of Yb-doped silica glass through the modification of MCVD process. *J. Non-Cryst. Solids* **2008**, *354*, 4737–4742. [CrossRef]
26. Naji, A.; Hamida, B.A.; Cheng, X.; Mahdi, M.A.; Harun, S.; Khan, S.; Al-Khateeb, W.; Zaidan, A.; Zaidan, B.; Ahmad, H. Review of Erbium-doped fiber amplifier. *Int. J. Phys. Sci.* **2011**, *6*, 4674–4689.
27. Aubry, M.; Mescia, L.; Morana, A.; Robin, T.; Laurent, A.; Mekki, J.; Marin, E.; Ouerdane, Y.; Girard, S.; Boukenter, A. Temperature influence on the radiation responses of erbium-doped fiber amplifiers. *Phys. Status Solidi (a)* **2021**, *218*, 2100002. [CrossRef]
28. Chu, T.; Wang, P.; Zhu, C. Modeling of active fiber loop ring-down spectroscopy considering gain saturation behavior of EDFA. *J. Light. Technol.* **2019**, *38*, 966–973. [CrossRef]
29. Bolshtyansky, M.; Wysocki, P.; Conti, N. Model of temperature dependence for gain shape of erbium-doped fiber amplifier. *J. Light. Technol.* **2000**, *18*, 1533. [CrossRef]
30. Zhou, Y.; Gai, N.; Wang, J.; Chen, F.; Yang, G. Effect of hydroxyl groups on Er^{3+}-doped bismuth-borate glass and fiber. *J. Lumin.* **2009**, *129*, 277–282. [CrossRef]
31. Mescia, L.; Bia, P.; Girard, S.; Ladaci, A.; Chiapperino, M.A.; Robin, T.; Laurent, A.; Cadier, B.; Boutillier, M.; Ouerdane, Y. Temperature-Dependent Modeling of Cladding-Pumped $\mathrm{Er}^{3+}/\mathrm{Yb}^{3+}$-Codoped Fiber Amplifiers for Space Applications. *J. Light. Technol.* **2018**, *36*, 3594–3602. [CrossRef]
32. Jazi, M.K.; Shahi, S.; Hekmat, M.; Saghafifar, H.; Khuzani, A.; Khalilian, H.; Baghi, M. The evaluation of various designs for a C and L band superfluorescent source based erbium doped fiber. *Laser Phys.* **2013**, *23*, 065104. [CrossRef]